Identification and Analysis of Collisional Breakup in Natural Rain

LEO PIO D'ADDERIO

Department of Physics and Earth Sciences, University of Ferrara, Ferrara, Italy

FEDERICO PORCÙ

Department of Physics and Astronomy, University of Bologna, Bologna, Italy

ALI TOKAY

Joint Center for Earth Systems Technology, University of Maryland, Baltimore County, Baltimore, and NASA Goddard Space Flight Center, Greenbelt, Maryland

(Manuscript received 10 October 2014, in final form 6 May 2015)

ABSTRACT

Numerous laboratory and numerical studies have been dedicated to understanding collisional breakup as one of the most important processes in rain formation. The present study aims to identify when, in natural rain, collisional breakup is dominant and thus able to modify the shape of the raindrop size distribution (DSD), up to the equilibrium DSD. To this end, an automated objective algorithm has been developed and applied to a total of more than 6000 two-minute-averaged DSDs. Since breakup is mostly observed in heavy precipitation, the method was applied to the DSDs where rain rate was above 5 mm h^{-1}. The selected breakup DSDs had good agreement with those predicted to be the equilibrium DSD by different theoretical models. The equilibrium DSD was found in a variable fraction of the total samples (0%–7%), confirming that the onset of equilibrium is a rare event in natural rain. The occurrence of a DSD in which breakup is dominant and modifies the DSD but the equilibrium DSD is not reached is higher (15%–47%). The gamma distribution, which has been widely used in the parameterization of observed size spectra, had a poor fitting in breakup-induced DSD, especially in the 1.0–2.6-mm-diameter interval. This can impact applications for which the parameterization of DSD is needed, such as in the retrieval of a DSD integral parameter (such as rain rate) from active remote sensor data.

1. Introduction

The characteristics of the raindrop size distribution (DSD) have been widely studied since Marshall and Palmer (1948), which introduced a specific version of exponential distribution for the observed size spectra based on Marshall et al.'s (1947) measurements of raindrop records on dyed filter papers. Marshall and Palmer (1948) added that their measurements were in fair agreement with a similar study by Laws and Parsons (1943). Since the impact-type Joss–Waldvogel disdrometer (Joss and Waldvogel 1969) became commercially available during the early 1970s, there have been numerous studies on the representation of observed DSD in a mathematical form. Among those studies, the gamma distribution (Ulbrich 1983) has been widely used and is adopted for retrieval of DSD from spaceborne radar measurements, including the National Aeronautics and Space Administration (NASA) Tropical Rainfall Measuring Mission (TRMM) Precipitation Radar (Kozu et al. 2009) and the Global Precipitation Measurement (GPM) mission Dual-Frequency Radar (Seto et al. 2013). Meanwhile, advances in optics and radar technology resulted in newly designed disdrometers, which later became commercially available. The two-dimensional video disdrometer (Kruger and Krajewski 2002) and the laser-optical Particle Size Velocity (Parsivel) disdrometer (Löffler-Mang and Joss 2000) are based on optical principles, while the Precipitation Occurrence Sensor System (POSS; Sheppard 1990) and Pludix (Prodi et al. 2000) are low-power

Corresponding author address: Leo Pio D'Adderio, Department of Physics and Earth Science, University of Ferrara, Via Saragat 1, 44122 Ferrara, Italy.
E-mail: dadderio@fe.infn.it

DOI: 10.1175/JAS-D-14-0304.1

© 2015 American Meteorological Society

radars. The optical disdrometers measure the size and fall velocity of individual hydrometeors directly, while the radar-based disdrometers infer the size distribution in a relatively larger sampling volume. Comparative studies intend to demonstrate advantages and shortcomings of each disdrometer type (Krajewski et al. 2006; Tokay et al. 2013, 2014), so the error in physical interpretation and any other application of DSD can be assessed. The shape of the size distribution is highly variable not only because of the changes in rain intensity but also because of the physics of precipitation. Tokay and Short (1996) demonstrated the differences in DSD between the convective and stratiform rain at the same rain rate in the tropics. Similarly, the DSD exhibited different concentrations between small and large drops at the same reflectivity in the Amazon basin of Brazil between westerly and easterly regimes (Tokay et al. 2002). There have been distinct differences in DSD shape at the same reflectivity when rainfall is dominated through the collision–coalescence process in the presence of the shallow ice layer aloft and when rainfall is dominated though the riming process of the deep ice layer. The former is typically observed in rainfall of oceanic origin, while the latter is often seen in rainfall of continental origin (Tokay et al. 2008). The breakup is one of the main mechanisms that determine the DSD shape in natural rain. In particular, when a larger drop and a smaller drop collide and their collisional kinetic energy (CKE) is not dissipated by viscous motion of water molecules inside the coalesced drop but is able to overcome the surface tension, the drops break in smaller fragments. Undisturbed water drops can survive falling in air, reaching sizes from 6 up to 8 mm (Villermaux and Bossa 2010; Szakáll et al. 2010) and then break because of aerodynamical deformation. This is known as aerodynamical breakup, and it does not play an important role in natural DSD shape; Barros et al. (2010) showed evidence that the mean free path for a collision between two drops is comparable with the average distance a drop has to fall before having spontaneous breakup and that their setup does not correctly represent free-fall natural conditions.

The first laboratory studies on collisional breakup were made by McTaggart-Cowan and List (1975) setting up an aerodynamic drop accelerator to study collisions between 10 pairs of drops (ranging from 0.04- to 4.4-mm diameter) at terminal speed. With a similar setup, Low and List (1982a,b) and List et al. (2009) increased the spectrum of drop sizes in colliding pairs in order to cover a wider range of events. More recent laboratory studies focused on fragment distributions (Emersic and Connolly 2011) and aerodynamic breakup (Villermaux and Bossa 2010; Szakáll et al. 2010). McFarquhar (2004) used a box model to derive the equilibrium DSD where the mass is conserved. The resultant DSD had two peaks around 0.26 and 2.3 mm and a relative minimum around 1.6 mm, where coalescence and breakup were balanced. Prat and Barros (2007) followed Low and List (1982a,b) and McFarquhar (2004) parameterizations in a microphysical model and found a good agreement in peak location of DSD equilibrium, with higher discrepancies in the number of very small droplets (diameter below 0.2 mm). They also obtained a third peak around 0.8 mm when they used Low and List's (1982a) parameterization. By using a different modeling approach and introducing a new parameterization, Straub et al. (2010) found a stationary DSD with two peaks around 0.5 and 2.0 mm. It has to be mentioned that small differences in peak positions among modeling results could be due to different model approaches and rain processes kernels (Prat and Barros 2007; Prat et al. 2012).

Evidence of the breakup influence on experimental DSD shape was observed by Zawadzki and De Agostinho Antonio (1988) and Willis and Tattelman (1989), with a bimodal DSD at rain rates higher than 100 and 200 mm h^{-1}, respectively. For much lower rain rates, Wilson and Barros (2014) estimated the relative impact of coalescence and breakup in natural rain at different altitudes. Porcù et al. (2013, 2014) measured DSDs at different altitudes and observed the breakup evidence with a bimodal DSD shape. They found that peak diameters were different from those of McFarquhar (2004) and had altitude dependency.

The three-parameter gamma distribution (Ulbrich 1983) is frequently used to model the DSD. Willis and Tattelman (1989), for instance, fitted the experimental DSDs with gamma distribution and computed the squared error for each measured distribution over a wide range of rainfall. They found that the gamma distribution is generally a good approximation, but, in the presence of the bimodal DSD, a more complex function is needed to represent the observed size spectrum. Cao and Zhang (2009) calculated bias and fractional error for different moment estimators of measured and gamma-modeled DSD. Their results show that generally middle-moment estimators—namely second, third, and fourth order—produce lower error, except when the DSD is not well fitted by the gamma distribution; in that case, the order of moment estimators depends on the selected integral parameter (i.e., third and sixth order can be used for the dual-polarized radar parameters).

The aim of this work is to analyze the DSD of natural rain to identify the signature of collisional breakup. For this purpose, we set up an automatic breakup identification algorithm that can be applied to experimental DSD data. The paper is structured as follows. Section 2

describes the characteristics of instruments and the datasets used in this study. The algorithm is described in section 3. The application of the algorithm to disdrometer datasets that were collected at various climatic regimes is reported in section 4. This section highlights the characteristics of DSD where breakup is dominant (and the equilibrium DSD is reached) and where it is not. Section 5 presents the comparison between experimental DSDs and gamma-fitted distributions, while the conclusions and future perspectives are presented in the last section.

2. Instruments and measurement campaigns

a. *Two-dimensional video disdrometer (2DVD)*

The 2DVD (Kruger and Krajewski 2002; Schönhuber et al. 2007) measures size, fall velocity, and shape of each hydrometeor that falls in its cross section, which is nominally 10 cm × 10 cm. It is equipped with two high-speed line-scan cameras (A and B) with orthogonal projections. The matching images from camera A and camera B are critical to obtain geometrical properties of the hydrometeor correctly. The hydrometeor size is estimated by counting the number of pixels occupied in each image in both cameras. The fall velocity of hydrometeors is directly related to the elapsed time between the two planes. In that regard, each 2DVD is calibrated with dropping metal spheres. In the presence of rain, the deviation of measured fall speed from Gunn and Kinzer's (1949) observations may hint at a calibration error or oscillatory behavior, as documented in Thurai et al. (2013). The secondary drops either due to the splashing or dripping at the edge of sampling cross section or mismatching are filtered out using a threshold where the measured fall speed is faster or slower than plus or minus 50% of the Gunn and Kinzer (1949) observations. Recent comparative studies revealed that the 2DVD often underestimates the drop concentration for sizes less than 0.5 mm in diameter (Tokay et al. 2013). For the present study, the drops with diameters between 0 and 10 mm are considered. To construct the size distribution, the bin size has been set to 0.2 mm and the sampling time to 1 min.

b. *Parsivel^2*

Parsivel^2 is the third generation of the laser-optical disdrometer. Parsivel was originally developed by PM Tech Inc., Germany (Löffler-Mang and Joss 2000). Later, OTT redesigned Parsivel mainly as a present-weather sensor for the transportation industry. Parsivel^2 is an upgraded version of Parsivel, and measurement accuracy at both the small and large drop ends is noticeably better in the new model (Tokay et al. 2014; Angulo-Martinez and Barros 2015). It has a laser diode (wavelength 780 nm) that generates a horizontal flat beam. The measurement area is nominally 54 cm^2. When a hydrometeor passes through the laser beam, it produces an attenuation proportional to its size. A relationship between the attenuation and the particle size is used to estimate the particle size. Parsivel^2 can measure particles of diameters up to about 25 mm and classifies them in 32 size classes of different width. The instrument also estimates the hydrometeor terminal velocity by measuring the time necessary for the particle to pass through the laser beam. As for the 2DVD, the Parsivel sampling time is also set to 1 min.

c. *Field campaigns*

The 2DVD data in this study were collected in six different field campaigns that were conducted under the GPM ground validation program (Hou et al. 2014). The number of instruments, the seasonality, the location, and the duration of the field studies vary from one site to another and are listed in Table 1. The first column of Table 1 also reports the city of the operational center of each campaign, while the instruments were collocated at various distances ranging from 100 m to about 110 km. The sizes of the datasets used in this study ranged from about 140 min during the Light Precipitation Validation Experiment (LPVEx; Tokay 2010) to about 4200 min during the Iowa Flooding Studies (IFloodS; Tokay 2013), as noted in Table 1. The Parsivel^2 data were collected in three of the six field campaigns, and the dataset sizes range from about 6500 min for the Wallops Flight Facility (Wallops; A. Tokay 2013, unpublished data) to about 9400 min for the Integrated Precipitation and Hydrology Experiment (IPHEx; Barros et al. 2014; Tokay 2014). For the other three sites, Parsivel (the previous version of Parsivel^2) is operated. Since the data quality of Parsivel^2 is significantly better than that of the old model (Tokay et al. 2014), we decided not to use the Parsivel data.

3. Collisional drop breakup identification algorithm

Based on theoretical and laboratory studies, the modification of the DSD shape from a single peak to two or three peaks is a clear indication of collisional drop breakup (Low and List 1982a; McFarquhar 2004; Prat and Barros 2007).

During the evolution of a rain event, the collision–coalescence and the collisional breakup dominate the resultant DSD at the ground. If there is a dry layer underneath the precipitation, evaporation also plays a significant role, especially at the small-drop end. The

TABLE 1. Overview of field campaigns.

Field campaign	Location	Duration	2DVD		Parsivel[2]	
			No. of instruments	No. of 1-min obs (>5 mm h^{-1})	No. of instruments	No. of 1-min obs (>5 mm h^{-1})
IFloodS (Iowa City and Waterloo, Iowa)	42°N, 92°W	May–Jun 2013	6	4222	14	7520
MC3E (Ponca City, Oklahoma)	36°N, 97°W	Apr–Jun 2011	7	968	—	—
Wallops (Wallops Island, Virginia)	37°N, 75°W	Jul 2013–Mar 2014	6	3912	6	6446
Alabama (Huntsville, Alabama)	35°N, 87°W	Dec 2009–Jun 2010	3	904	—	—
IPHEx (Asheville, North Carolina)	35°N, 83°W	May–Jun 2014	5	2114	12	9316
LPVEx (Helsinki, Finland)	60°N, 24°E	Sep–Dec 2010	3	134	—	—

coalescence produces an increase of medium-size drops, while the key feature in breakup is the presence of a relative minimum followed by a relative maximum. McFarquhar (2004) and Pratt and Barros (2007) reported a relative minimum and maximum in the DSD spectrum around 1.5 and 2.5 mm, respectively. The relative minimum and maximum position in the DSD spectrum may be explained through CKE analysis, as defined by Low and List (1982a):

$$\mathrm{CKE} = \frac{\pi\rho}{12}\frac{D_S^3 D_L^3}{D_S^3 + D_L^3}(V_L - V_S)^2,$$

where D is the drop's diameter and V is the drop's terminal velocity, while the subscripts L and S indicate large and small colliding drops, respectively. Figure 1 shows the CKE values as a function of D_L and D_S.

Low and List (1982a) stated that collisional breakup can take place when CKE $> 5\,\mu$J, but it is more effective in modifying the DSD when a drop of a size corresponding to the relative minimum (i.e., around 1.5 mm) collides with a drop larger than 3 mm, resulting in a number of small fragments and one large fragment of a size slightly smaller than the large colliding drop. Breakup between larger size pairs may also occur as long as provided CKE $> 5\,\mu$J, but it has less impact on the DSD shape because of the lower number of such collisions. For collisions with CKE $> 5\,\mu$J, the breakup can occur or not, depending on other collision characteristics, such as eccentricity (Schlottke et al. 2010; Szakáll et al. 2014). As a result of breakup, drops around 1.5 mm are depleted, while there is an increase of small drops (less than 1 mm in diameter) and an increase of drops around 2–3 mm so that an inflection point shows up in the DSD between 1.0 and 2.6 mm. The peak at small diameters is more marked than the one at larger size. It should be noted that it is impossible to recognize the breakup signature only by this feature because they could be due to other factors that occur in and above the precipitation layer (Radhakrishna and Rao 2009). Not even the second peak, at larger diameter, represents a feature sufficient to recognize the breakup because it can also be a product of coalescence (McFarquhar 2004).

The inflection point in the range 1.0–2.6 mm is the main feature in DSD shape considered here to identify cases where the breakup is dominant. When the equilibrium DSD is reached, the inflection point lies between a local minimum and a local maximum, and the DSD has positive slope around it. For this reason, the slope of the DSD in the 1.0–2.6-mm range is analyzed: the inflection point is searched for over a rather wide

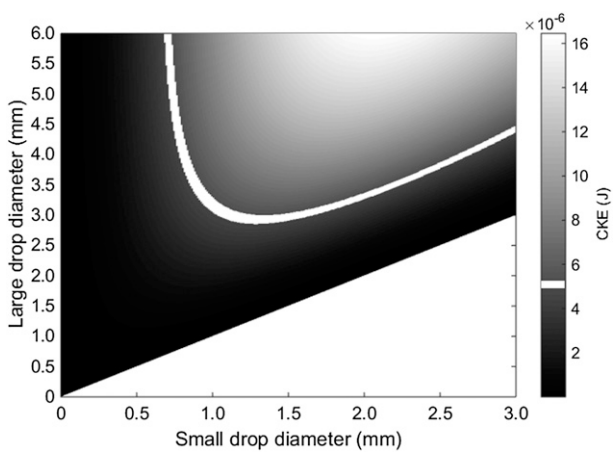

FIG. 1. CKE as a function of small and large colliding drops. The white line marks the 5-μJ threshold.

diameter range to take into account the expected uncertainties in disdrometer measurement and in the simulated DSDs, used here as a reference to identify breakup signature in the DSD. Figure 2 shows three examples of DSDs that, in the range 1.0–2.6 mm, have positive (Fig. 2a) or negative slopes (Figs. 2b,c). The dotted lines give a qualitative indication of the highest slope (HS) direction, while the HS value computed by the algorithm is reported in the Fig. 2 legends.

The automated algorithm is designed to identify the strength of the breakup signal in the DSD. It is developed primarily for 2DVD data, which are sampled at a uniform size bin, but it is also applied to Parsivel[2] DSD, where the raw output contains drop counts at uneven size bins. The algorithm consists of five steps:

- The linear best fit of the considered DSD is calculated over a five diameter bins from smaller (starting point) to larger diameters.
- Four different starting points are considered between 1.0 and 1.6 mm with steps of 0.2 mm. This results in four linear relationships that fit the DSD between 1.0 and 2.6 mm.
- The HS of the four linear best fits is considered as a reference to label the DSD.
- The individual DSDs are sorted from the lowest (negative) to the highest (possibly positive) HS value. HS ranges from -4.56 to $1.97\,\mathrm{m^{-3}\,mm^{-2}}$.
- A total of six classes are introduced based on HS. Most of the DSDs have slopes between 0 and $-2\,\mathrm{m^{-3}\,mm^{-2}}$, and this range is divided into four classes with an interval of $0.5\,\mathrm{m^{-3}\,mm^{-2}}$ (classes 2–5), and the remaining two classes are defined with $\mathrm{HS} > 0\,\mathrm{m^{-3}\,mm^{-2}}$ (class 1) and with $\mathrm{HS} < -2\,\mathrm{m^{-3}\,mm^{-2}}$ (class 6).

The algorithm analyzes the DSD spectrum between 1.0- and 2.6-mm diameter by computing the slope of the linear best fit (see Fig. 2, dotted lines) and ranks the DSDs accordingly. The use of the slope of the linear fit was revealed, after sensitivity studies, to be reliable and robust in identifying the changes in slope of DSD, and it avoids recognizing as breakup signature isolated spikes due to the natural DSD variability at such short time scales, especially if discrete differential operators are used.

The 1-min disdrometer observations are averaged over 2 min to have a more stable sampling and to maintain a large-enough dataset. A minimum rainfall threshold of $5\,\mathrm{mm\,h^{-1}}$ is adopted to eliminate light rain, since breakup is expected to take place mainly in heavy rain (Li et al. 2009). This also prevents the analysis of light-rain DSDs that can present sharp discontinuities because of the low number of drops and because the algorithm, which assumes the continuity of the DSD between 1.0 and 2.6 mm, may fail.

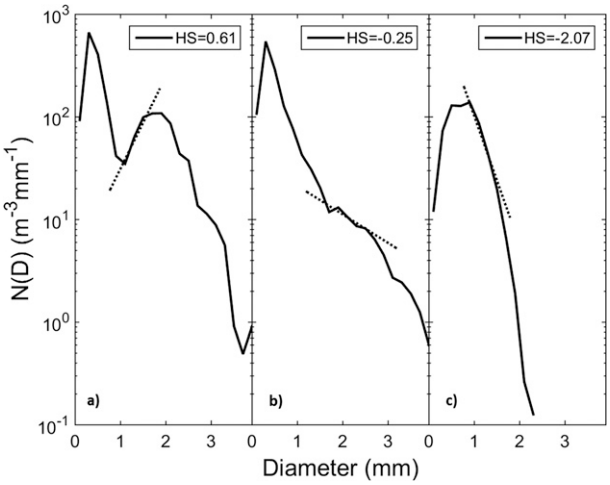

FIG. 2. Three examples of DSD with different values of HS of the linear fit (dotted lines). The slope lines do not represent the reported HS value because of axis shrinking.

As a matter of fact, many other mechanisms occurring in the cloud or precipitation layers could be responsible for multiple peaks in experimental DSD: the breakup of ice particles (Valdez and Young 1985; Brown 1988), the overlapping of rain shafts (Radhakrishna and Rao 2009), the coexistence of ice and supercooled water (Zawadzki et al. 2001), and the complex interplay of all these mechanisms (Radhakrishna and Rao 2009). Our point here is that, when breakup is dominant in the rain layer, it is able to substantially modify the DSD, and the system may reach the equilibrium DSD, while the effects of other mechanisms are more evident in cases of light precipitation rates.

4. Raindrop size distribution measurements

Figure 3 shows the 2DVD-derived DSDs averaged on the six HS classes defined in the previous section for the six field campaigns. The number of 2-min averages (herein referred to as samples) for each class is also given.

A concave-down DSD shape with a single peak is observed in all six sites for classes 5 and 6. The peak occurred at a diameter between 0.5 and 1.0 mm, and the relatively low concentration of smaller-size drops is primarily attributed to the underestimation of small drops by 2DVD (Tokay et al. 2013). For the remaining four classes, a well-defined peak occurred at 0.3 mm. For class 1, the DSD had a sharp decrease in concentration from the peak to around 1.0 mm, followed by a plateau where the concentration slightly increases without changing significantly with size, until 2.0 mm. A secondary maximum was observed at around 2 mm at most of the sites, followed by exponential decrease with increasing drop sizes. The DSDs with positive HS (class 1)

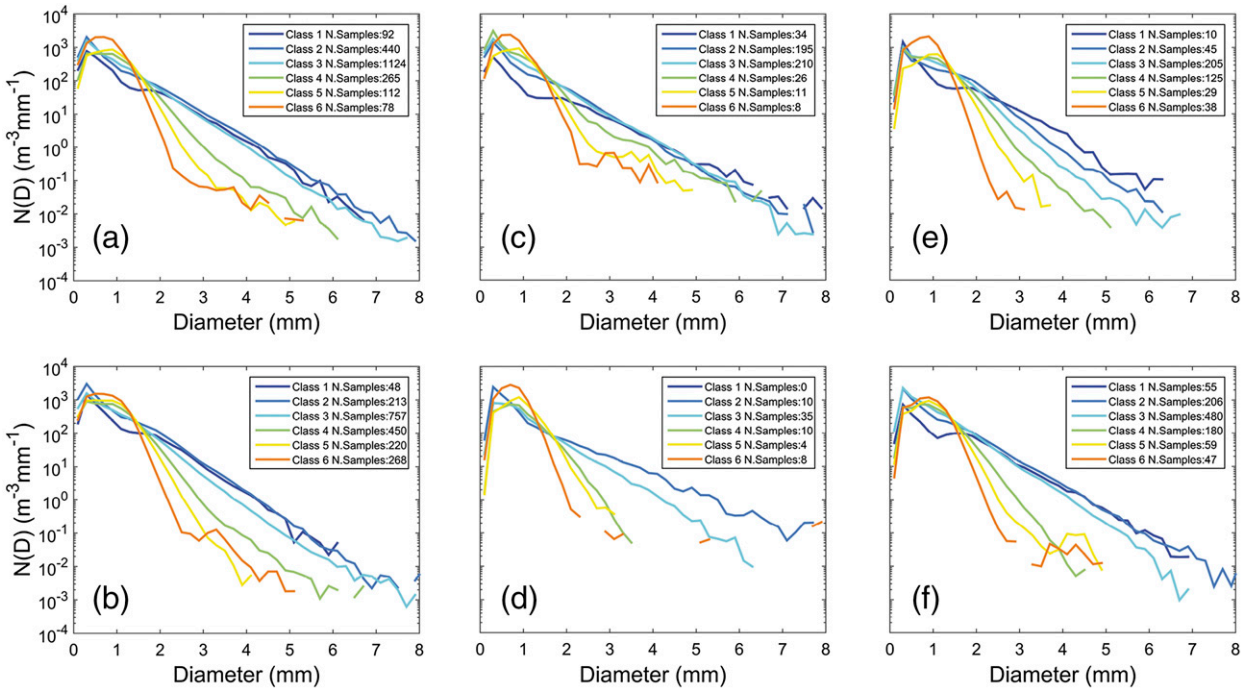

FIG. 3. Mean DSD for each HS class for each field campaign from 2DVD data: (a) IFloodS, (b) Wallops, (c) MC3E, (d) LPVEx, (e) Alabama, and (f) IPHEx. The number of samples of all HS classes is also reported.

have good agreement with those obtained by different models and defined as the equilibrium DSD (McFarquhar 2004; Prat and Barros 2007; Straub et al. 2010). Thus, class 1 is labeled as the equilibrium DSD. Class 2 shows a sharp decrease in drop concentration from the peak to 1.0 mm, followed by relatively slower decrease between 1.0 and 2.0 mm. It represents samples where breakup is significantly present, as witnessed by the inflection point on the class 2 curves in Fig. 3, but the equilibrium DSD is not reached. Class 2 can be seen as a transition between the equilibrium DSD and the DSD where the breakup is negligible with respect to other processes. Classes 3 and 4 have the exponential slope from peak distribution to the largest observables sizes, wherein the slope is sharper in class 4 than in class 3. When the drop concentrations for each size interval fall below 0.1 drops $m^{-3}\,mm^{-1}$, the DSD exhibits one or more discontinuities, mostly observed for drop diameters larger than 2 mm.

Figure 4 reports the cloud envelope of the mean DSD plus and minus one standard deviation of each of the six HS classes for the IFloodS dataset. The cloud envelope follows the trend of the mean DSD, and the changing in DSD shape from class 1 (Fig. 4a) to class 6 (Fig. 4f) is evident. The width of cloud envelope decreases both from class 1 to class 6 and from smaller to larger diameters. When the drop concentration is very low, about 1 $m^{-3}\,mm^{-1}$, the variance of distribution of the number of drops corresponding to those diameter classes is too high, and the cloud envelope diverges.

Table 2 reports the percentage of samples in each HS class for each dataset. The DSDs have positive HS values in a low percentage of cases, marking the fact that the equilibrium DSD is rare in natural rain. The percentage values depend on the season of experiment and climatic characteristics of the regions. The maximum occurrence for class 1 was 7%, based on 2DVD observations during the Midlatitude Continental Convective Clouds Experiment (MC3E; Tokay 2011), which was carried out during the spring of 2011. In contrast, class-1 2DVD observations were 2.4% at Wallops, where the experiment period was mainly during autumn 2013 and winter 2013/14. Continental showers dominated the precipitation events during MC3E, while widespread stratiform precipitation was mainly observed at Wallops. The higher occurrence of breakup-dominated DSD in convective rain is also confirmed by Prat and Barros (2009), showing that the time scale to equilibrium is much shorter for heavy rainfall.

Combining the classes 1 and 2, the percentage reaches up to about 47% during MC3E. This means that breakup is more frequent during convective episodes, but only in a few cases (the 7% in class 1) is the equilibrium DSD reached. High percentage values were also

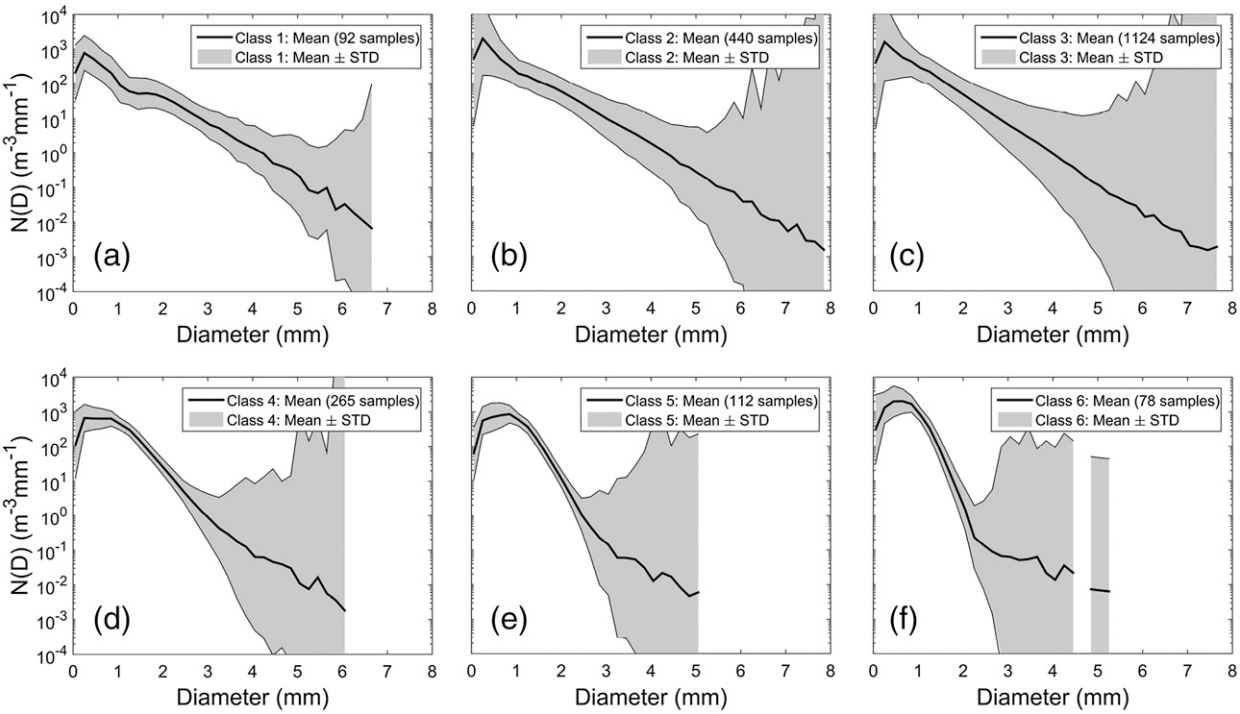

FIG. 4. Cloud envelope of mean DSD plus and minus one standard deviation (STD) for each HS class for the IFloodS dataset. The number of samples of each HS class is also reported.

observed for both classes 1 and 2 during IPHEx and IFloodS, in which the experiments focused on springtime flooding over orographic and flat areas, respectively.

LPVEx had the lowest occurrences for classes 1 (0%) and 2 (14.9%). This experiment was designed for observations of light rain that frequently occurs during autumn at high latitudes, and this is additional proof that breakup takes place mostly during convective rain. In Alabama (A. Tokay 2011, unpublished data), the percentages were relatively low for classes 1 and 2. Although most of the observations were during spring and early summer, few cases of convective rainfall were included. The rain rate and reflectivity recorded were below 10 mm h^{-1} and 36 dBZ in most cases.

The HS-based classification described above is designed for disdrometer observations where the bin width is uniform. The performance of the identification algorithm was tested for Parsivel^2 observations where the bin width is not uniform and doubles from 0.129 to 0.257 mm at around 1.3 mm. This particular diameter is within the range of size bins used by the algorithm to compute the HS value.

Figure 5 reports the mean DSD for each HS class obtained from Parsivel^2 data for IFloodS, IPHEx, and Wallops. The results are in good agreement with the findings based on 2DVD: class 1 shows the DSD equilibrium, particularly during IFloodS and IPHEx, and class 2 identifies the samples where the breakup is able to modify the DSD shape. The similarity of features of DSD in each class between 2DVD and Parsivel^2 reveals that the HS-based algorithm is not limited to a disdrometer where the size bin is uniform. However, the percentage occurrence for classes 1 and 2 was much less in Parsivel^2 than in 2DVD (Table 2). This is mainly as a result of the larger width of DSD bins, which results in a smoother DSD curve and indicates that this instrument characteristic does not allow for recognizing a large portion of breakup cases.

Finally, the results reported in Figs. 3 and 5 point out that the inflection point, when present, is found in the range 1–2.6 mm, regardless of season, location, and instrument type. This is also confirmed by previous works on natural rain in different conditions (Willis and Tattelman 1989; Zawadzki and De Agostinho Antonio 1988; Porcù et al. 2014).

5. Gamma model distribution

The three-parameter gamma distribution (Ulbrich 1983) is widely used to parameterize the DSD. In particular, the parameters of the gamma distribution are retrieved from dual-polarized radar measurements (Bringi et al. 2003, 2004; Adirosi et al. 2014) and from single- and dual-frequency spaceborne radar

TABLE 2. Percentage of occurrence for each HS class for each dataset.

	IFloodS		MC3E	Wallops		Alabama	LPVEx	IPHEx	
Class	2DVD	Parsivel	2DVD	2DVD	Parsivel	2DVD	2DVD	2DVD	Parsivel
1	4.5	0.8	7.0	2.4	1.0	2.2	0	5.3	1.0
2	20.8	15.4	40.3	10.9	6.6	10.0	14.9	19.5	7.5
3	53.2	58.7	43.3	38.7	41.2	45.3	52.3	45.4	40.7
4	12.5	15.6	5.4	23.0	28.1	27.7	14.9	17.0	32.3
5	5.3	4.5	2.3	11.3	11.4	6.4	6.0	8.4	9.6
6	3.7	5.0	1.7	13.7	11.7	8.4	11.9	4.4	8.9

measurements (Kozu et al. 2009; Seto et al. 2013; Liao et al. 2014). The parametric form of a gamma distribution is expressed as follows:

$$N(D) = N_0 D^{\mu} e^{-\Lambda D},$$

where N_0 ($\mathrm{mm}^{-1}\,\mathrm{m}^{-3}$) is the intercept parameter, μ is the shape parameter that can assume both positive and negative values, and Λ (mm^{-1}) is the slope parameter and assumes positive values only. The method of moments is applied to calculate the parameters, and the nth moment of a DSD is calculated as follows:

$$M_n = N_0 \frac{\Gamma(\mu + n + 1)}{\Lambda^{\mu+n+1}} = \int_0^{\infty} N(D) D^n \, dD,$$

where Γ represents the complete gamma function.

Figure 6 shows four different gamma distributions as a function of μ and Λ. The shape parameter determines the concavity, while Λ determines the slope of the distribution. Positive values of μ determine downward concavity in cases with a low concentration of small drops, while negative values indicate upward concavity with abundant small drops. Higher values of Λ indicate narrow distribution in the absence of large drops, while wider distributions result in lower Λ values. A visual comparison between Figs. 3–5 and Fig. 6 reveals that the gamma distribution is not the best model for the DSD in presence of dominant breakup. This study does not seek an alternative model for a better fit to the breakup-induced DSD; rather, it evaluates the differences between the DSDs either dominated or not by breakup and the goodness of the gamma parameterization.

We used the method of moments of second, third, and fourth orders (M234) to estimate the gamma parameters, following Cao and Zhang (2009), who pointed out the advantages of M234 with respect to the other moments in fitting DSD with a gamma distribution. After the computation of nondimensional parameter:

$$\eta = \frac{M_2 M_4}{M_3^2},$$

the gamma parameters μ, Λ, and N_0 are expressed as follows:

$$\mu = \frac{4 - 3\eta}{\eta - 1}, \quad \Lambda = \frac{M_2}{M_3(\eta - 1)}, \quad \text{and} \quad N_0 = \frac{M_2 \Lambda^{\mu+3}}{\Gamma(\mu + 3)}.$$

The normalized gamma distribution is also used to parameterize the DSD. If the normalization is done with respect to the total concentration N_T and the liquid water content W, the respective intercept parameters N_T^* and N_W are expressed as follows:

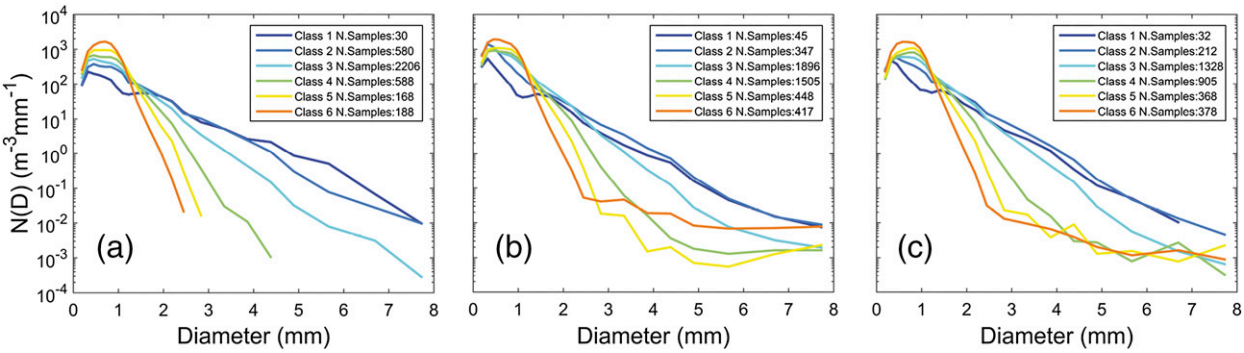

FIG. 5. Mean DSD for each HS class for each field campaign from Parsivel^2 data. (a) IFloodS, (b) IPHEx, and (c) Wallops. The number of samples of all HS classes is also reported.

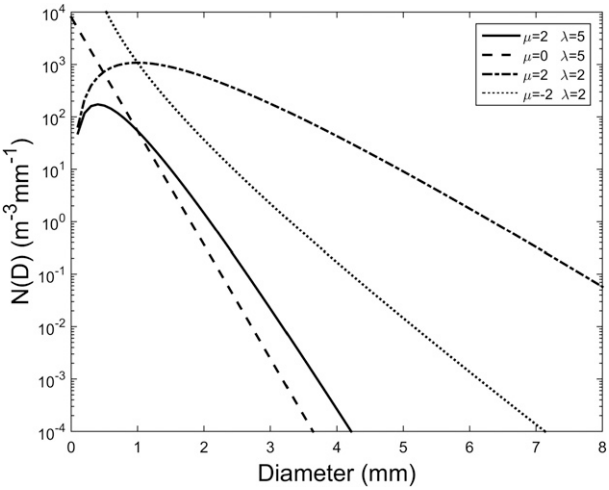

FIG. 6. Gamma distribution as a function of μ and Λ.

$$N_T^* = \frac{N_T}{D_m} \quad \text{and} \quad N_W = \frac{256}{\pi\rho_W}\frac{10^3 W}{D_m^4},$$

where ρ_w is the density of water, while D_m is the ratio between the fourth and third moments of DSD:

$$D_m = \frac{\int_{D_{\min}}^{D_{\max}} N(D)D^4\,dD}{\int_{D_{\min}}^{D_{\max}} N(D)D^3\,dD}.$$

a. Correlations

The Pearson correlation coefficient is calculated between the experimental 2-min-averaged DSD and the corresponding estimated gamma distribution to determine the applicability of the gamma fit at six different HS classes. The correlation is also calculated for the size interval 1.0–2.6 mm, where the algorithm computes the slope of the DSD to assess the impact of breakup. Figure 7 shows the correlation coefficients between the experimental DSDs and the estimated gamma distributions for the IFloodS 2DVD dataset, which is the largest dataset. Considering the entire size spectrum, the majority of observations have correlations above 0.8 for classes 3–6, while the correlations have a relatively wider range for classes 1 and 2 (Fig. 7a). For the selected size interval of 1.0–2.6 mm, the correlations remained above 0.9 for classes 3–6, while class 1 exhibited evenly distributed correlations from near 0 to 1 (Fig. 7b). This shows that the gamma distribution often fails in approximating breakup-dominated DSDs, and the same applies to other single-maximum functions (such as the lognormal distribution). Class 2, which is the transition between the equilibrium DSD and the DSD where the breakup is negligible with respect to other processes, has high correlations both above 0.9 and between 0.6 and 0.9. It should be added that the low correlation could be partially due to the differences between observed and fitted spectra in small and large drop ends. Since M234 is used, the fitting in both ends of the size spectrum may substantially deviate from the observations. If the observed spectrum has a large number of small drops and/or a presence of large drops, the correlations are expected to be relatively low.

b. Integral rainfall and size distribution parameters

The parametric form of size distribution is often derived from disdrometer observations without visually inspecting the DSD. In that regard, it is important to identify the breakup-based DSD parameters if they are different than nonbreakup DSD parameters. The sensitivity of the selected rain and size distribution parameters to the HS classes is presented for the IFloodS 2DVD data, the largest dataset among all sites. The analysis was also conducted for the other field campaigns' datasets, but the results are not shown in this study because the findings were similar.

Table 3 reports the mean and standard deviation of selected DSD parameters for each class. The mean value of D_m and maximum drop diameter $D_{\max}$ decreases from class 1 to class 6, as does the standard deviation, while the two normalized intercept parameters N_T^* and N_W increase. Both rain rate R and reflectivity Z have the highest mean values for class 2, which shows also the highest standard deviation. Class 1 has mean R and Z mean close to those of class 2 but with lower standard deviation.

The distributions of D_m and $D_{\max}$, as well as N_T^* and N_W, had different characteristics at different classes. The values of D_m and $D_{\max}$ decreased from class 1 to class 6, while the reverse was true for logarithmic values of N_T^* and N_W (Figs. 8a–d). The low values of $D_{\max}$ and D_m indicate narrow DSD, while high values of N_T^* and N_W reveal large concentrations of small and midsize drops for classes 5 and 6. This is in agreement with the mean DSD in Figs. 3a–5a. The increase in $D_{\max}$ and D_m is more gradual from class 3 to class 1, coinciding with relatively small changes in the width of the size distribution in Figs. 3a–5a. The decrease in N_T^* and N_W is also gradual from class 3 to class 1.

Rain rate, which is moment 3.67 of the DSD, did not show any trend from class 1 to class 6 (Fig. 8e). Reflectivity, which is the sixth moment of DSD, decreased from class 1 to class 6 (Fig. 8f). Classes 2 and 3 had larger sample sizes and show wide variations in both rain rate and reflectivity. Class 1 had relatively smaller sample size and was bounded between 5 and 30 mm h^{-1} for rain rate and between 36 and 51 dBZ for reflectivity. Models

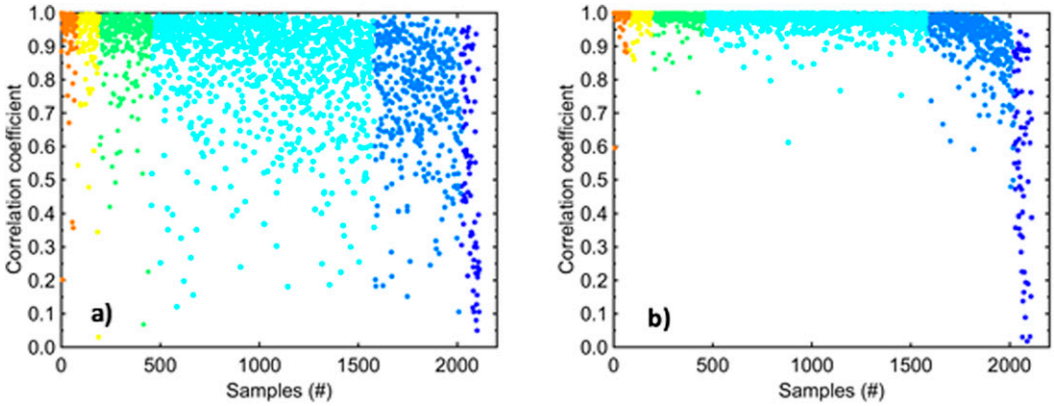

FIG. 7. Pearson correlation coefficient between the experimental DSD and the estimated gamma distribution for (a) the whole DSD spectrum and (b) the 1.0–2.6-mm-diameter range, for the IFloodS dataset. The samples are ordered from the lowest to the highest HS value. Colors refer to the HS class, as in Fig. 3.

find different rain-rate thresholds for the onset of equilibrium DSD, generally varying between 10 and 50 mm h^{-1}, depending on the kernel, parameterization, and time scale used (McFarquhar 2004; Prat and Barros 2007; Prat et al. 2012). We remark that models use much shorter time scales (1–10 s), while we have 2 min, and we are in natural rain, where more complex interplay between other mechanisms takes place. Overall, none of the computed DSD parameters, if considered alone, can be used to classify breakup versus nonbreakup DSD, but they can be additional indicators to screen out situations where collisional breakup is not able to modify significantly the DSD shape (i.e., no modification of the DSD shape due to the breakup process when $Z < 36$ dBZ).

6. Conclusions

An unprecedented disdrometer dataset has been analyzed to study the collisional breakup in natural rain, developing and applying an algorithm to identify breakup in experimental DSD. Six different measurement campaigns, where three to seven 2DVDs were operated, provided approximately 6000 two-minute DSDs with rainfall rate higher than 5 mm h^{-1}. In addition, a large Parsivel^2 dataset from three field campaigns was analyzed to test the applicability of a breakup identification algorithm to disdrometers with uneven bin sizes. Indeed, the success of the algorithm to rank DSDs according to relative impact of breakup, for both uniform and nonuniform bin-width disdrometer measurements, is a key accomplishment of this study.

The algorithm defined six classes based on the highest slope (HS) of DSD between 1.0 and 2.6 mm, as represented by a linear fit. Class 1 indicated the dominant role of breakup, in agreement with what different model and laboratory studies describe as equilibrium DSD, characterized by a two-peak shape, while class 2 is considered as a transition between the equilibrium DSD and the DSD where breakup is not a relevant feature. This study showed that equilibrium DSD is not commonly reached in natural rain, as expected by modeling studies, based on the percentage occurrence of class 1 (between 0% and 7% of the events among the different campaigns, depending on season and latitude), but breakup occurrence is significant if class 1 and class 2 are considered. There were also distinct differences in DSDs between classes 5 and 6 and classes 1–4. Classes 5 and 6 exhibited relatively narrow distribution with more small and midsize drops than the other classes.

This study showed that gamma distribution, which is employed to retrieve size distribution parameters from dual-frequency radar measurements onboard the GPM

TABLE 3. Mean plus or minus standard deviation of selected DSD parameters for each class during IFloodS.

Class	R (mm h^{-1})	Z (dBZ)	D_m (mm)	$D_{\max}$ (mm)	$\log(N_T^*)$ (m^{-3} mm^{-1})	$\log(N_W)$ (m^{-3} mm^{-1})
1	10.6 ± 6.8	43.2 ± 3.8	2.4 ± 0.6	4.6 ± 1.0	2.3 ± 0.4	3.2 ± 0.4
2	15.8 ± 16.3	44.7 ± 4.4	2.2 ± 0.4	4.5 ± 1.0	2.7 ± 0.4	3.4 ± 0.4
3	12.5 ± 15.8	42.3 ± 4.0	1.9 ± 0.3	4.1 ± 0.8	2.7 ± 0.4	3.6 ± 0.3
4	7.6 ± 2.6	36.3 ± 2.3	1.5 ± 0.2	3.2 ± 0.7	2.7 ± 0.2	3.9 ± 0.2
5	6.8 ± 2.2	34.1 ± 2.1	1.3 ± 0.2	2.8 ± 0.7	2.8 ± 0.2	4.2 ± 0.2
6	7.1 ± 2.1	31.7 ± 1.4	1.1 ± 0.1	2.2 ± 0.3	3.1 ± 0.3	4.5 ± 0.2

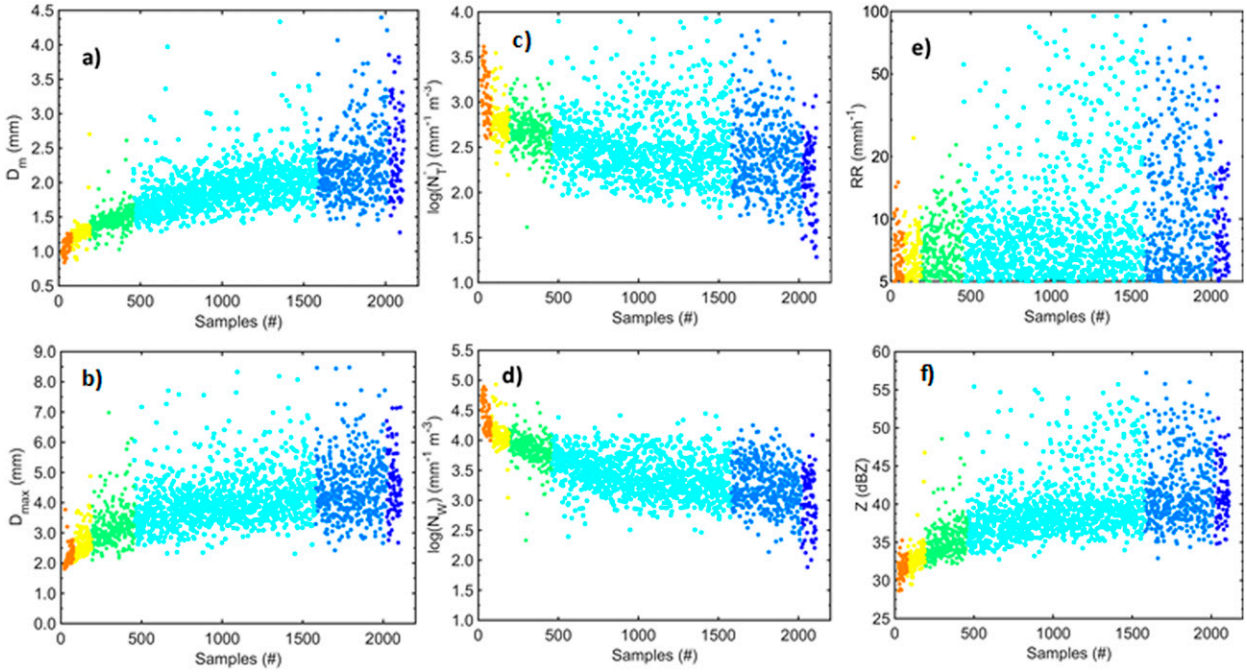

FIG. 8. Distribution of the selected DSD parameters as a function of the sample's number, ranked from the lowest to the highest HS value: (a) D_m, (b) $D_{\max}$, (c) $\log(N_T^*)$, (d) $\log(N_W)$, (e) R, and (f) Z. Different colors refer to the six HS classes, as in Fig. 3

core satellite, as well as every other one-peak distribution, does not represent well the DSD with dominant breakup. The parameters of the gamma distribution, on the other hand, had an increasing or decreasing trend from classes 1 to 6, but there is no quantitative signal between DSDs dominated or not by breakup: they can only give an additional indication.

In the future, more detailed analysis can be carried out on different aspects highlighted by this work. The investigation of which mathematical function can represent DSD with dominant breakup provides guidance for the DSD retrieval from radar and/or satellite observations. A systematic time-series analysis of HS values can allow understanding within the rain event when breakup is more likely to be dominant, with respect to the cloud lifetime. The continental convection in the presence of lightning may produce a higher percentage of breakup than the oceanic convection in the absence of lightning.

Acknowledgments. This study was partially funded by the European Commission (Call FP7-ENV-2007-1 Grant 212921) as part of the CEOP-AEGIS project coordinated by the Université de Strasbourg, and by the "Bando per soggiorno all'estero" of the University Institute for Higher Studies, (IUSS–Ferrara 1391) of the University of Ferrara. Thanks to Patrick N. Gatlin of the NASA Marshall Space Flight Center and Matthew Wingo of the University of Alabama at Huntsville for maintenance of 2DVD during the NASA Global Precipitation Measurement (GPM) mission ground validation field campaigns led by Walter Petersen of the NASA Wallops Flight Facility. We thank Robert Meneghini of the NASA Goddard Space Flight Center and Xiaowen Li of Morgan State University for useful discussions. The efforts of Ana Barros (Duke University) and two anonymous reviewers contributed to increase the quality of this paper.

REFERENCES

Adirosi, E., E. Gorgucci, L. Baldini, and A. Tokay, 2014: Evaluation of gamma raindrop size distribution assumption through comparison of rain rates of measured and radar-equivalent gamma DSD. *J. Appl. Meteor. Climatol.,* **53,** 1618–1635, doi:10.1175/JAMC-D-13-0150.1.

Angulo-Martinez, M., and A. P. Barros, 2015: Measurement uncertainty in rainfall kinetic energy and intensity relationships for soil erosion studies: An evaluation using PARSIVEL disdrometers in the southern Appalachian Mountains. *Geomorphology,* **228,** 28–40, doi:10.1016/j.geomorph.2014.07.036.

Barros, A. P., O. P. Pratt, and F. Y. Testik, 2010: Size distribution of raindrops. *Nat. Phys.,* **6,** 232, doi:10.1038/nphys1646.

——, and Coauthors, 2014: NASA GPM-Ground Validation: Integrated Precipitation and Hydrology Experiment 2014 science plan. NASA Tech. Rep., 64 pp., doi:10.7924/G8CC0XMR.

Bringi, V. N., V. Chandrasekar, J. Hubbert, E. Gorgucci, W. L. Randeu, and M. Schoenhuber, 2003: Raindrop size distribution in different climatic regimes from disdrometer and dual-

polarized radar analysis. *J. Atmos. Sci.,* **60,** 354–365, doi:10.1175/1520-0469(2003)060<0354:RSDIDC>2.0.CO;2.

——, T. Tang, and V. Chandrasekar, 2004: Evaluation of a new polarimetrically based *Z–R* relation. *J. Atmos. Oceanic Technol.,* **21,** 612–623, doi:10.1175/1520-0426(2004)021<0612:EOANPB>2.0.CO;2.

Brown, P. S., Jr., 1988: The effects of filament, sheet, and disk breakup upon the drop spectrum. *J. Atmos. Sci.,* **45,** 712–718, doi:10.1175/1520-0469(1988)045<0712:TEOFSA>2.0.CO;2.

Cao, Q., and G. Zhang, 2009: Errors in estimating raindrop size distribution parameters employing disdrometer and simulated raindrop spectra. *J. Appl. Meteor. Climatol.,* **48,** 406–425, doi:10.1175/2008JAMC2026.1.

Emersic, C., and P. J. Connolly, 2011: The breakup of levitating water drops observed with a high speed camera. *Atmos. Chem. Phys.,* **11,** 10 205–10 218, doi:10.5194/acp-11-10205-2011.

Gunn, R., and G. D. Kinzer, 1949: The terminal velocity of fall water drops in stagnant air. *J. Meteor.,* **6,** 243–248, doi:10.1175/1520-0469(1949)006<0243:TTVOFF>2.0.CO;2.

Hou, A. Y., and Coauthors, 2014: The Global Precipitation Measurement Mission. *Bull. Amer. Meteor. Soc.,* **95,** 701–722, doi:10.1175/BAMS-D-13-00164.1.

Joss, J., and A. Waldvogel, 1969: Raindrop size distribution and sampling size errors. *J. Atmos. Sci.,* **26,** 566–569, doi:10.1175/1520-0469(1969)026<0566:RSDASS>2.0.CO;2.

Kozu, T., T. Iguchi, T. Kubota, N. Yoshida, S. Seto, J. Kwiatkowski, and Y. N. Takayabu, 2009: Feasibility of raindrop size distribution parameter estimation with TRMM precipitation radar. *J. Meteor. Soc. Japan,* **87A,** 53–66, doi:10.2151/jmsj.87A.53.

Krajewski, W. F., and Coauthors, 2006: DEVEX–disdrometer evaluation experiment: Basic results and implications for hydrologic studies. *Adv. Water Resour.,* **29,** 311–325, doi:10.1016/j.advwatres.2005.03.018.

Kruger, A., and W. F. Krajewski, 2002: Two-dimensional video disdrometer: A description. *J. Atmos. Oceanic Technol.,* **19,** 602–617, doi:10.1175/1520-0426(2002)019<0602:TDVDAD>2.0.CO;2.

Laws, J. O., and D. A. Parsons, 1943: The relation of raindrop-size to intensity. *Eos, Trans. Amer. Geophys. Union,* **24,** 452–460, doi:10.1029/TR024i002p00452.

Li, X., W. Tao, A. P. Khain, J. Simpson, and D. E. Johnson, 2009: Sensitivity of a cloud-resolving model to bulk and explicit bin microphysical schemes. Part II: Cloud microphysics and storm dynamics interactions. *J. Atmos. Sci.,* **66,** 22–40, doi:10.1175/2008JAS2647.1.

Liao, L., R. Meneghini, and A. Tokay, 2014: Uncertainties of GPM DPR rain estimates caused by DSD parameterizations. *J. Appl. Meteor. Climatol.,* **53,** 2524–2537, doi:10.1175/JAMC-D-14-0003.1.

List, R., R. Nissen, and C. Fung, 2009: Effects of pressure on collision, coalescence, and breakup of raindrops. Part II: Parameterization and spectra evolution at 50 and 100 kPa. *J. Atmos. Sci.,* **66,** 2204–2215, doi:10.1175/2009JAS2875.1.

Löffler-Mang, M., and J. Joss, 2000: An optical disdrometer for measuring size and velocity of hydrometeors. *J. Atmos. Oceanic Technol.,* **17,** 130–139, doi:10.1175/1520-0426(2000)017<0130:AODFMS>2.0.CO;2.

Low, T. B., and R. List, 1982a: Collision, coalescence and breakup of raindrops. Part I: Experimentally established coalescence efficiencies and fragment size distributions in breakup. *J. Atmos. Sci.,* **39,** 1591–1606, doi:10.1175/1520-0469(1982)039<1591:CCABOR>2.0.CO;2.

——, and ——, 1982b: Collision, coalescence and breakup of raindrops. Part II: Parameterizations of fragment size distributions. *J. Atmos. Sci.,* **39,** 1607–1618, doi:10.1175/1520-0469(1982)039<1607:CCABOR>2.0.CO;2.

Marshall, J. S., and W. Palmer, 1948: The distribution of raindrops with size. *J. Meteor.,* **5,** 165–166, doi:10.1175/1520-0469(1948)005<0165:TDORWS>2.0.CO;2.

——, R. C. Langille, and W. Palmer, 1947: Measurement of rainfall by radar. *J. Meteor.,* **4,** 186–192, doi:10.1175/1520-0469(1947)004<0186:MORBR>2.0.CO;2.

McFarquhar, G. M., 2004: A new representation of collision-induced breakup of raindrops and its implications for the shapes of raindrop size distributions. *J. Atmos. Sci.,* **61,** 777–794, doi:10.1175/1520-0469(2004)061<0777:ANROCB>2.0.CO;2.

McTaggart-Cowan, J. D., and R. List, 1975: Collision and breakup of water drops at terminal velocity. *J. Atmos. Sci.,* **32,** 1401–1411, doi:10.1175/1520-0469(1975)032<1401:CABOWD>2.0.CO;2.

Porcù, F., L. P. D'Adderio, F. Prodi, and C. Caracciolo, 2013: Effects of altitude on maximum raindrop size and fall velocity as limited by collisional breakup. *J. Atmos. Sci.,* **70,** 1129–1134, doi:10.1175/JAS-D-12-0100.1.

——, ——, ——, and ——, 2014: Rain drop size distribution over the Tibetan Plateau. *Atmos. Res.,* **150,** 21–30, doi:10.1016/j.atmosres.2014.07.005.

Prat, O. P., and A. P. Barros, 2007: A robust numerical solution of the stochastic collection–breakup equation for warm rain. *J. Appl. Meteor. Climatol,* **46,** 1480–1497, doi:10.1175/JAM2544.1.

——, and ——, 2009: Exploring the transient behavior of *Z–R* relationships: Implications for radar rainfall estimation. *J. Appl. Meteor. Climatol.,* **48,** 2127–2143, doi:10.1175/2009JAMC2165.1.

——, ——, and F. Testik, 2012: On the influence of raindrop collision outcomes on equilibrium size distributions. *J. Atmos. Sci.,* **69,** 1534–1546, doi:10.1175/JAS-D-11-0192.1.

Prodi, F., A. Tagliavini, and F. Pasqualucci, 2000: Pludix: An X-band sensor for measuring hydrometeors size distributions and fall rate. *Proc. 13th Int. Conf. on Clouds and Precipitation,* Reno, NV, Int. Commission on Clouds and Precipitation, 338–339.

Radhakrishna, B., and T. N. Rao, 2009: Statistical characteristics of multipeak raindrop size distributions at the surface and aloft in different rain regimes. *Mon. Wea. Rev.,* **137,** 3501–3518, doi:10.1175/2009MWR2967.1.

Schlottke, J., W. Straub, K. Beheng, H. Gomaa, and B. Weigand, 2010: Numerical investigation of collision-induced breakup of raindrops. Part I: Methodology and dependencies on collision energy and eccentricity. *J. Atmos. Sci.,* **67,** 557–575, doi:10.1175/2009JAS3174.1.

Schönhuber, M., G. Lammer, and W. L. Randeu, 2007: One decade of imaging precipitation measurement by 2D-video-disdrometer. *Adv. Geosci.,* **10,** 85–90, doi:10.5194/adgeo-10-85-2007.

Seto, S., T. Iguchi, and T. Oki, 2013: The basic performance of a precipitation retrieval algorithm for the Global Precipitation Measurement Mission's single/dual-frequency radar measurements. *IEEE Trans. Geosci. Remote Sens.,* **51,** 5239–5251, doi:10.1109/TGRS.2012.2231686.

Sheppard, B. E., 1990: Measurement of raindrop size distributions using a small Doppler radar. *J. Atmos. Oceanic Technol.,* **7,** 255–268, doi:10.1175/1520-0426(1990)007<0255:MORSDU>2.0.CO;2.

Straub, W., K. Behenga, A. Seifert, J. Schlottke, and B. Weigand, 2010: Numerical investigation of collision-induced breakup of

raindrops. Part II: Parameterizations of coalescence efficiencies and fragment size distributions. *J. Atmos. Sci.,* **67,** 576–588, doi:10.1175/2009JAS3175.1.

Szakáll, M., S. K. Mitra, K. Diehl, and S. Borrmann, 2010: Shapes and oscillations of falling raindrops—A review. *Atmos. Res.,* **97,** 416–425, doi:10.1016/j.atmosres.2010.03.024.

——, S. Kessler, K. Diehl, S. K. Mitra, and S. Borrmann, 2014: A wind tunnel study of the effects of collision processes on the shape and oscillation for moderate-size raindrops. *Atmos. Res.,* **142,** 67–78, doi:10.1016/j.atmosres.2013.09.005.

Thurai, M., V. N. Bringi, W. A. Petersen, and P. N. Gatlin, 2013: Drop shapes and fall speeds in rain: Two contrasting examples. *J. Appl. Meteor. Climatol.,* **52,** 2567–2581, doi:10.1175/JAMC-D-12-085.1.

Tokay, A., 2010: Light Precipitation Validation Experiment (LPVEx) dataset. Accessed 1 March 2014. [Available online at http://trmm-fc.gsfc.nasa.gov/Disdrometer/LPVex/index.html.]

——, 2011: Midlatitude Continental Convective Cloud Experiment (MC3E) dataset. Accessed 1 March 2014. [Available online at http://trmm-fc.gsfc.nasa.gov/Field_Campaigns/MC3E/.]

——, 2013: Iowa Flood Studies (IFloodS) dataset. NASA GHRC, accessed 1 March 2014. [Available online at ftp://trmm-fc.gsfc.nasa.gov/Field_Campaigns/IFloodS/.]

——, 2014: Integrated Precipitation and Hydrology Experiment (IPHEx) dataset. Accessed 1 July 2014. [Available online at ftp://trmm-fc.gsfc.nasa.gov/Field_Campaigns/IPHEX/.]

——, and D. A. Short, 1996: Evidence from tropical raindrop spectra of the origin of rain from stratiform versus convective clouds. *J. Appl. Meteor.,* **35,** 355–371, doi:10.1175/1520-0450(1996)035<0355:EFTRSO>2.0.CO;2.

——, A. Kruger, W. Krajewski, P. A. Kucera, and A. J. Pereira Filho, 2002: Measurements of drop size distribution in the southwestern Amazon basin. *J. Geophys. Res.,* **107,** 8052, doi:10.1029/2001JD000355.

——, P. G. Bashor, E. Habib, and T. Kasparis, 2008: Raindrop size distribution measurements in tropical cyclones. *Mon. Wea. Rev.,* **136,** 1669–1685, doi:10.1175/2007MWR2122.1.

——, W. A. Petersen, W. Gatlin, and M. Wingo, 2013: Comparison of raindrop size distribution measurements by collocated disdrometers. *J. Atmos. Oceanic Technol.,* **30,** 1672–1690, doi:10.1175/JTECH-D-12-00163.1.

——, D. B. Wolff, and W. A. Petersen, 2014: Evaluation of the new version of the laser-optical disdrometer, OTT Parsivel2. *J. Atmos. Oceanic Technol.,* **31,** 1276–1288, doi:10.1175/JTECH-D-13-00174.1.

Ulbrich, C., 1983: Natural variations in the analytical form of the raindrop size distribution. *J. Climate Appl. Meteor.,* **22,** 1764–1775, doi:10.1175/1520-0450(1983)022<1764:NVITAF>2.0.CO;2.

Valdez, M. P., and K. C. Young, 1985: Number fluxes in equilibrium raindrop populations: A Markov chain analysis. *J. Atmos. Sci.,* **42,** 1024–1036, doi:10.1175/1520-0469(1985)042<1024:NFIERP>2.0.CO;2.

Villermaux, E., and B. Bossa, 2010: Size distribution of raindrops. *Nat. Phys.,* **6,** 232, doi:10.1038/nphys1648.

Willis, P. T., and P. Tattelman, 1989: Drop-size distributions associated with intense rainfall. *J. Appl. Meteor.,* **28,** 3–15, doi:10.1175/1520-0450(1989)028<0003:DSDAWI>2.0.CO;2.

Wilson, A. M., and A. P. Barros, 2014: An investigation of warm rainfall microphysics in the southern Appalachians: Orographic enhancement via low-level seeder–feeder interactions. *J. Atmos. Sci.,* **71,** 1783–1805, doi:10.1175/JAS-D-13-0228.1.

Zawadzki, I., and M. De Agostinho Antonio, 1988: Equilibrium raindrop size distributions in tropical rain. *J. Atmos. Sci.,* **45,** 3452–3459, doi:10.1175/1520-0469(1988)045<3452:ERSDIT>2.0.CO;2.

——, F. Fabry, and W. Szyrmer, 2001: Observations of supercooled water and secondary ice generation by a vertically pointing X-band Doppler radar. *Atmos. Res.,* **59–60,** 343–359, doi:10.1016/S0169-8095(01)00124-7.